Full length article

Interface dominated mechanical properties of ultra-fine grained and nanoporous Au at elevated temperatures

A. Leitner [a], V. Maier-Kiener [b], J. Jeong [c, e], M.D. Abad [d, 1], P. Hosemann [d], S.H. Oh [e], D. Kiener [a, *]

[a] Department Materials Physics, Montanuniversität Leoben, Jahnstraße 12, A-8700, Leoben, Austria
[b] Department Physical Metallurgy and Materials Testing, Montanuniversität Leoben, Roseggerstraße 12, A-8700, Leoben, Austria
[c] Center for Integrated Nanostructure Physics, Institute for Basic Science (IBS), Suwon 16419, Republic of Korea
[d] Department of Nuclear Engineering, University of California, Berkeley 4155, Etcheverry Hall, Berkeley, CA, 94720, USA
[e] Department of Energy Science, Sungkyunkwan University (SKKU), Suwon 16419, Republic of Korea

A R T I C L E   I N F O

A B S T R A C T

Modern design and engineering of highly efficient devices and machines demand innovative materials to satisfy requirements such as high strength at low density. The purpose of this study was to oppose the mechanical properties and deformation behavior of ultra-fine grained Au to those of nanoporous Au, to study the influence of different types of interfaces. Microstructural investigations of the foam surrendered a ligament size of ~100 nm which themselves consist of 70 nm grains in average, while the ultra-fine grained gold features a mean grain size of 325 nm. Nanoindentation lends itself as a convenient technique to obtain material properties at ambient as well as high temperature conditions. In this work, a substantial indentation test series was performed in order to determine hardness, Young's modulus, strain-rate sensitivity and activation volume at room and elevated temperatures up to 300 °C. On account of the small characteristic dimensions, high hardness values were noted for both materials, which rapidly drop at elevated temperature. Additionally, an enhanced strain-rate sensitivity accompanied by low activation volumes was determined at room temperature, which further increased at elevated temperatures. This behavior is associated with thermally activated interactions between dislocations and interfaces. For nanoporous Au, due to the presence of free surfaces, a considerable increase of hardness was observed upon annealing. This can be attributed to a reduced number of mobile dislocations in the material after annealing, as supported by implemented porosity maps on indent cross-sections, showing distinct differences for tests at varying temperature.

1. Introduction

Metals with characteristic structure dimensions approaching the sub-micron scale are known to differ in their mechanical properties compared to their coarse grained counterparts, especially due to the restrained state of dislocations. This issue, first described by Hall and Petch [1,2], in addition with recently observed hardening effects caused by annealing [3,4], put material classes such as ultra-fine grained (UFG) and nanocrystalline (NC) materials in the spotlight of various fields of applications. Grain boundary strengthening provides the opportunity to increase the strength without undesired effects on the endurable strain of the metal, and thus is widely used for high-performance components. Light-weight constructions on the other hand, are considered to be the key to high efficiency and energy-saving technologies, which are indispensable in the 21st century. Hence, it seems natural to investigate not only UFG bulk materials, but in particular nanoporous (NP) structures which combine the assets of small structure dimensions and light-weight materials. It is not surprising that studies on NP Au revealed exceptional high ligament strengths at room temperature [5—10], since it is well known that strength increases with decreasing structure size, often demonstrated for nano-pillars or nanowires [11—15]. Recently, there was also evidence that NP materials possess a high radiation resistance resulting from self-healing mechanisms

* Corresponding author.
E-mail addresses: alexander.leitner@unileoben.ac.at (A. Leitner), verena.maier-kiener@unileoben.ac.at (V. Maier-Kiener), jiwonjeong@skku.edu (J. Jeong), manuel.abad@gmail.com (M.D. Abad), peterh@berkeley.edu (P. Hosemann), sanghooh@skku.edu (S.H. Oh), daniel.kiener@unileoben.ac.at (D. Kiener).
[1] Now: University College of Dublin, School of Mechanical and Materials Engineering, Belfield, Dublin 4, Ireland.

[16], making them suitable for nuclear applications. The governing deformation mechanisms in such NP structures, in particular at elevated temperatures, are thus of great interest in order to understand their mechanical behavior.

Face-centered cubic (fcc) UFG metals are reported to exhibit multiple deformation mechanisms, such as dislocation emission from grain boundaries [17].Likewise grain boundary diffusion or micro shear banding can play a crucial role [18,19], and grain boundary sliding is known to occur at high temperature (HT) [18,20,21]. The dominating mechanism can be indicated by a noticeable strain-rate sensitivity corresponding to low activation volumes [22–29]. Certainly, this raises the question whether the type of interface exerts a significant influence on the mechanical behavior, since the models of the mentioned deformation mechanisms are based on bulk materials with a high number of grain boundaries. Therefore, the present study will investigate the different behavior of the NP and UFG state of Au to contrast grain boundaries with free surfaces, at RT as well as elevated temperatures up to 300 °C. Nanoindentation proves to be an optimal technique to extract mechanical properties [30], but also rate-dependent parameters, such as the strain-rate sensitivity m and the activation volume V^*[22,31–34], accompanied by minimal material consumption for testing.

Through a unique fabrication route by powder compaction and severe plastic deformation using High Pressure Torsion (HPT) temperature-stable UFG Au bulk samples as well as a NP Au foam with well-defined microstructure will be produced. Additionally, the deformation morphology will be unfolded by Focused Ion Beam (FIB) cross sections of indents, for the first time allowing verification of the dominating deformation mechanisms by the appearance of the plastic deformation underneath an indent. This will enable us to demonstrate that the interface type as well as the temperature have a major impact on the mechanical behavior and rate-dependent properties of nanostructured gold.

2. Experimental details

2.1. Sample fabrication and microstructure analysis

For this study, spherical Au powder (Alpha Aesar GmbH & Co KG) with a purity of 99.96% and an average particle size of 5.5–9.0 μm was used as a base material. The powder was poured into a copper ring, which in turn was glued on an HPT anvil before. Subsequently the powder was consolidated and deformed via HPT [35,36] to produce UFG Au disks with a diameter of 8 mm and a height of 0.8–1 mm. Likewise, a Au/Fe powder mixture (50/50 vol %) was densified to create a nanostructured composite [37–39], where the spherical Fe powder (obtained from Merck KGaA) features a purity of 99.9% with particle sizes < 10 μm. Since the formation of supersaturated phases after extensive severe plastic deformation has been observed [38], all samples were annealed at 300 °C for 1 h in a vacuum furnace (SERIES XRETORT, Xerion Advanced Heating Ofentechnik GmbH, Germany) to allow a reduction of the forced mixing. The pure UFG Au samples were annealed the same way in order to maintain comparable material conditions for both material types.

Subsequently, the HPT disks were ground from one side to 0.4–0.5 mm thickness to eliminate surface artefacts and reach the most homogenous zone of the sample. Next, Au/Fe specimens underwent a selective etching process to remove the Fe and obtain a novel nanoporous Au structure, similar to a procedure recently described to produce NP Cu [37]. For this purpose, a 5 wt% hydrochloric acid served as an etchant, in which the Fe in the composite was entirely dissolved after 24 h at 55 °C, leaving behind a Au foam with ~50% porosity. Finally, UFG and NP samples were annealed at 100 °C, 200 °C and 300 °C to study the microstructure stability.

The resultant microstructures were characterized using a scanning electron microscope (SEM; LEO type 1525, Carl Zeiss GmbH, Germany) combined with Electron Backscatter Diffraction (EBSD, EDAX Inc. Mahwah, USA). For the latter a 15° misorientation angle was set as threshold to differentiate low-angle from high-angle grain boundaries. An ultra-fine grained structure was revealed for compact Au samples with an average grain size of about 325 nm at room temperature (RT) (Fig. 1a). As evident from Fig. 1a–d and Fig. 2a, minor grain coarsening can be observed after high temperature (HT) annealing up to 300 °C. Energy dispersive X-ray (EDX) spectra show that the UFG Au disks contain small amounts of Cu (<1 at.%), which most likely originates from the copper ring used in the production process via powder consolidation.

SEM micrographs illustrate the NP topology of the Au foam after tests at the inscribed temperatures (Fig. 1e–h). The foam features a porosity of approximately 50% and ligaments with an average diameter of about 100 nm at RT. Using EBSD, it is shown that the ligaments themselves consist on average of approximately 70 nm diameter small grains with a narrow size distribution, see Fig. 1i. Information from the black area was not considered, since the image quality of the Kikuchi patterns in this zone falls below a critical value of 35%, and therefore an accurate determination of the grain structure could not be guaranteed. While a slight coarsening of grains takes place upon annealing, the ligament diameter remains rather unaltered (Fig. 1e–l), evaluated quantitatively in Fig. 2. The grain size of the foam may exceed the ligament's diameter, as intersections where ligaments converge are not considered in the analysis of the diameter. Several EDX scans performed at different areas show that despite the preceded annealing up to 5.5 at.% Fe is still remaining within the Au matrix.

2.2. Nanoindentation

2.2.1. Experimental setup

Depth sensing nanoindentation enables the determination of fundamental mechanical properties and parameters for the indication of the predominating deformation mechanism expending minimal material volumes. The experiments were performed using a Micro Materials NanoTest Platform 3 (Micro Materials, UK) nanoindentation device including a hot stage option. Common Berkovich tips were used, made from diamond for room temperature (RT) and from cubic boron nitride (cBN) for elevated temperature testing. Both tip materials are well-suited for HT testing since no tip/sample interaction is expected [40]. Calibrations of the indenter tips were conducted on fused silica according to the method proposed by Oliver and Pharr [30] to maintain an accurate area function and machine compliance. For high temperature measurements the sample was fixed with a ceramic adhesive (Omegabond 600, Omega Engineering Inc., Stamford, USA), likewise a reference sample was mounted. The indenter cabinet was purged with a reductive protective gas (hydrogen/argon mixture) in order to avoid any oxidational effects on the material. In addition to the thermocouples preinstalled on the nanoindenter device, an additional one was externally mounted on the surface of the reference sample to double-check the temperature conditions as close to the sample as possible.

A Nanoindenter G200 (Keysight Technologies, USA) featuring a continuous stiffness measurement (CSM) option was used to double-check the obtained RT indentation values by conducting CSM constant strain-rate (0.05 s^{-1}) measurements and nanoindentation strain-rate jump tests [32].

2.2.2. Testing procedure

Displacement controlled (DC) runs with proportional load ramps (equivalent to a constant strain-rate) with 5 s dwell time at maximum load were performed to obtain the hardness (H) and
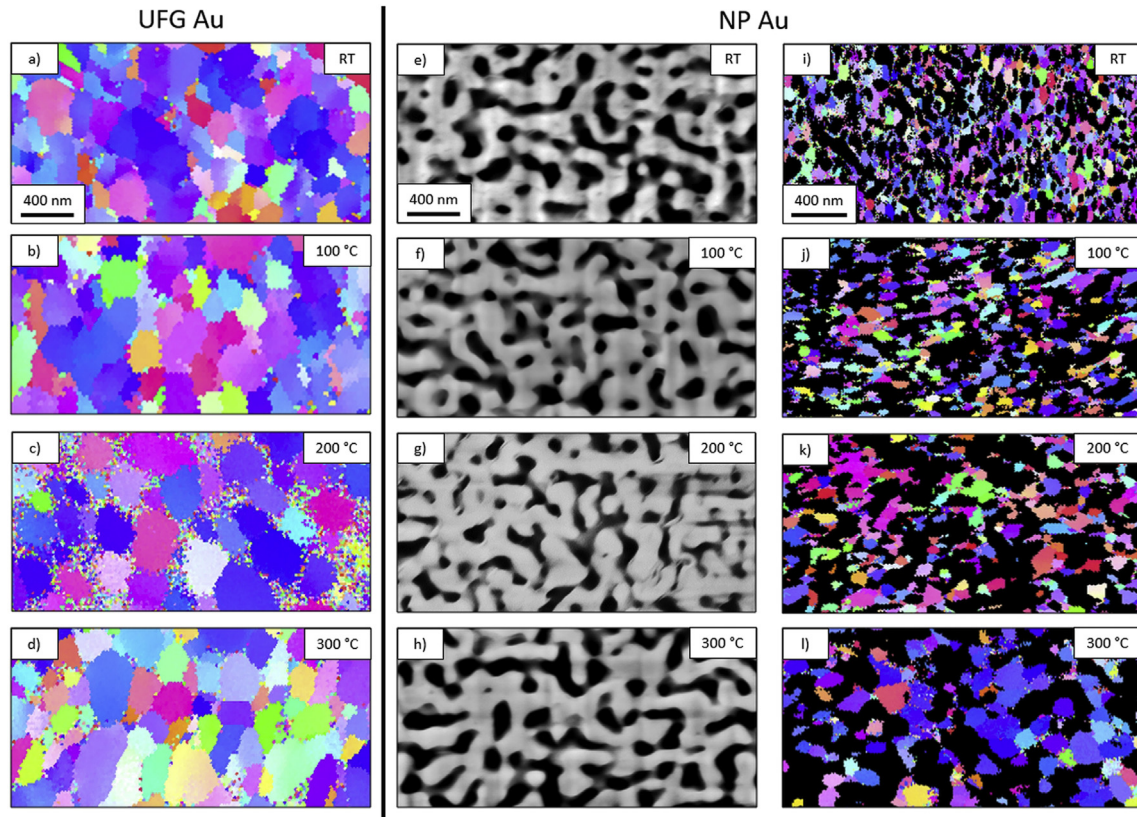
Fig. 1. Microstructural characteristics at RT and after annealing at the inscribed temperature up to 300 °C. EBSD scans, represented in a)–d) reveal the grain size and structure of UFG Au. Images e)–h) display SEM micrographs of the ligaments of NP Au and i)–l) the EBSD data of the foam.
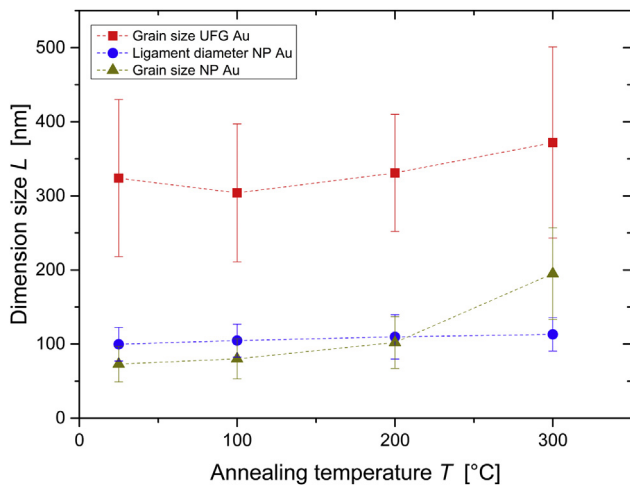

Fig. 2. Evolution of grain size and ligament diameter for UFG Au and NP Au upon annealing to 300 °C.
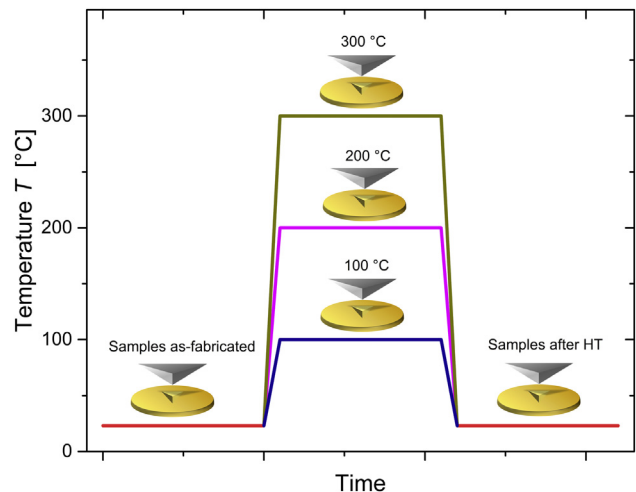

Fig. 3. Overview of the temperature profile for nanoindentation testing. Indenter symbols imply that the test was carried out at the assigned condition.

reduced modulus (E_r) following the method proposed by Oliver and Pharr [30]. In addition, load controlled (LC) tests with longer dwell times of 200 s were executed to determine the strain-rate sensitivity m and activation volume V^*, which were inferred from relaxation data of the hold segment, recently elaborately described by other authors [22,33,37,41]. Exemplary load-displacement curves are displayed in the appendix (Fig. A1). At least 10 indents were performed for each condition, and an overview of the testing temperature profile is depicted in Fig. 3. Starting at RT and further increasing temperature in steps of 100 °C until reaching 300 °C,

which corresponds to a homologous temperature range from 0.22 to 0.43. Supplementary RT measurements were conducted prior and after HT experiments in order to check for changes of the material or setup, respectively.

A penetration depth of 2000 nm for NP Au was supposed to be reasonable to comprise a sufficient number of ligaments. For UFG Au the maximum depth was reduced to 1000 nm, still covering about 100 grains in the tested volume. Indentation tests where thermal drift exceeded ±0.3 nm/s were identified and not considered in the later data analysis.

The reference measurements on the G200 nanoindentation device were conducted in DC mode with CSM to 2000 nm displacement into the surface to obtain mechanical properties at RT. In order to obtain m and V^*, strain rate jump tests were performed between strain-rate levels of 0.05 s^{-1}, 0.01 s^{-1} and 0.005 s^{-1}.

2.2.3. Analysis

The hardness and Young's modulus were obtained following the conventional procedure first described by Oliver and Pharr [30]. The strain-rate sensitivity m for a constant temperature T can be determined by rewriting the well-known power-law relation between strain-rate $\dot{\varepsilon}$ and stress σ[28,42] to

$$m = \left(\frac{\partial \ln H}{\partial \ln \dot{\varepsilon}} \right)_T, \tag{1}$$

since H is proportional to the indentation flow stress $\sigma_{f,i}$ via the constraint factor $H = \sigma_{f,i} \cdot C^*$. From this, it follows that the slope of the double logarithmic Norton plot is the reciprocal of m and hence can be plotted in dependence of the corresponding indentation flow stress. At a constant load, the resultant time/displacement curve during the dwell period can provide the required data [22,33], see Fig. 4.

Last but not least, the activation volume V^* can be determined based on the fundamental thermodynamic relation for the Gibbs free energy

$$V^* = -\left(\frac{\partial \Delta G}{\partial \tau} \right)_T. \tag{2}$$

For thermally activated deformation mechanisms and by taking into account the von Mises yield criterion, the activation volume may be written as [24].

$$V^* = C^* \cdot \sqrt{3} \cdot k_b \cdot T \cdot \frac{1}{m \cdot H}. \tag{3}$$

Frequently, V^* is divided by b^3, with b being the Burgers vector of the tested material. In the case of gold $b = 2.884 \cdot 10^{-10}$ m.

For porous media, Gibson and Ashby established a relation between macroscopic foams and bulk properties [43], which are often applied to microscopic foams too, even though their validity for ultra-fine porous or nanoporous foams with higher densities is still under debate [8,10,44–46]. These equations allow calculation of the flow stress and Young's modulus of the ligaments based on the bulk properties:

$$\sigma_f^* = C_1 \cdot \sigma_{f,s} \cdot \left(\frac{\rho^*}{\rho_s} \right)^p, \tag{4}$$
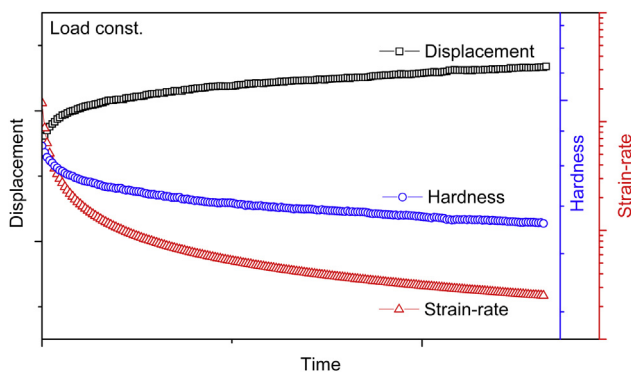

Fig. 4. Time profile of displacement, hardness and strain-rate during a dwell segment, used to determine strain-rate sensitivity m and activation volume V^*.

$$E^* = C_2 \cdot E_s \cdot \left(\frac{\rho^*}{\rho_s} \right)^q, \tag{5}$$

with $\sigma_{f,s}$ as the flow stress, E_s the Young's modulus and ρ_s the density of a solid bulk sample. The flow stress σ_f^*, Young's modulus E^* and density ρ^* refer to the porous foam. C_1, C_2,p and q are constants ascribed to cell geometry and cell deformation ($C_1 = 0.3$, $C_2 = 1$, $p = 1.5$, $q = 2$) [43].

For NP Au the value of ν has controversially been discussed in the past. While in some studies ν is assumed to be zero [5,9,10], experiments of several other authors indicate an average ν of about 0.2 [6,47,48]. Lately, this value was confirmed again in an extensive study of tension and compression tests of nanoporous Au [8,47], thus $\nu = 0.2$ will be used in the present work. C^* strongly depends on ν and changes from 1 ($\nu = 0$) to about 2.5 ($\nu = 0.2$) [43], ending up in lower indentation flow stresses. Thus, all presented stress data on NP Au can be regarded as a lower bound.

2.3. Implementation of porosity maps

Since the stress field beneath an indenter tip is not homogenous, the occurring deformation is not necessarily self-evident either. Cross-sections of indents were prepared with a focused ion beam (FIB, LEO-1540XB, Carl Zeiss GmbH, Germany) to examine the deformation appearance beneath the surface. The local densification of NP Au samples was analyzed through porosity maps. For this purpose, a python script was written to execute the following necessary steps. First the SEM images (8-bit greyscale) are converted to binary b/w images, in which the ratio of black and white pixels can be ascribed to the global porosity of the foam (Fig. 5a and b). To validate that an insensitive binarization threshold was used and the porosity maps display a realistic structure. Two markers having 0% and 100% porosity, respectively, were artificially added in an image, which should be clearly visible in the final map (Fig. 5c). Subsequently, a 500 nm × 500 nm box scans the image for local porosity with a step size of around 10 nm (corresponding to 1 px) to gain maximum resolution (Fig. 5d). This results in about three million porosity data points per image. Those are written in a 2-dimensional array, corresponding to the center coordinates of the of the analysis box, from which a densification colormap is created (Fig. 5e). Since the actual densification and not the inhomogeneity of the foam itself should be displayed, a deviation of ±5% around the mean relative density (measured in an unaffected zone) is displayed in white. Notably, an outer frame of half the box width, indicated in Fig. 5c, cannot be analyzed and is therefore neglected. Finally, the original image is automatically aligned with the porosity map to avoid any mismatch. The result in Fig. 5e confirms that the expected bulk porosity of 50%, as well as variations of the porosity, in this case the artificial markers, are detected properly. Therefore, this tool will be used later to analyze the densification of NP Au during nanoindentation at different temperatures. A more detailed study of the influence of numerical parameters such as threshold, box size and step size is given in Appendix C.

3. Results and analysis

3.1. Young's modulus and hardness

Fig. 6 demonstrates the trends of H and E as a function of temperature. For UFG Au the hardness shows a continuous decrease from $H = 1.58 \pm 0.04$ GPa at RT to $H = 0.22 \pm 0.01$ GPa at 300 °C, which equates to 14% of the RT value. At ambient temperature the Young's modulus reaches a value of $E = 88.0 \pm 2.0$ GPa, which eventually decreases to a level as low as $E = 54.3 \pm 2.7$ GPa (62% of E_{RT}) at 300 °C (Fig. 6a). When samples are measured again at RT
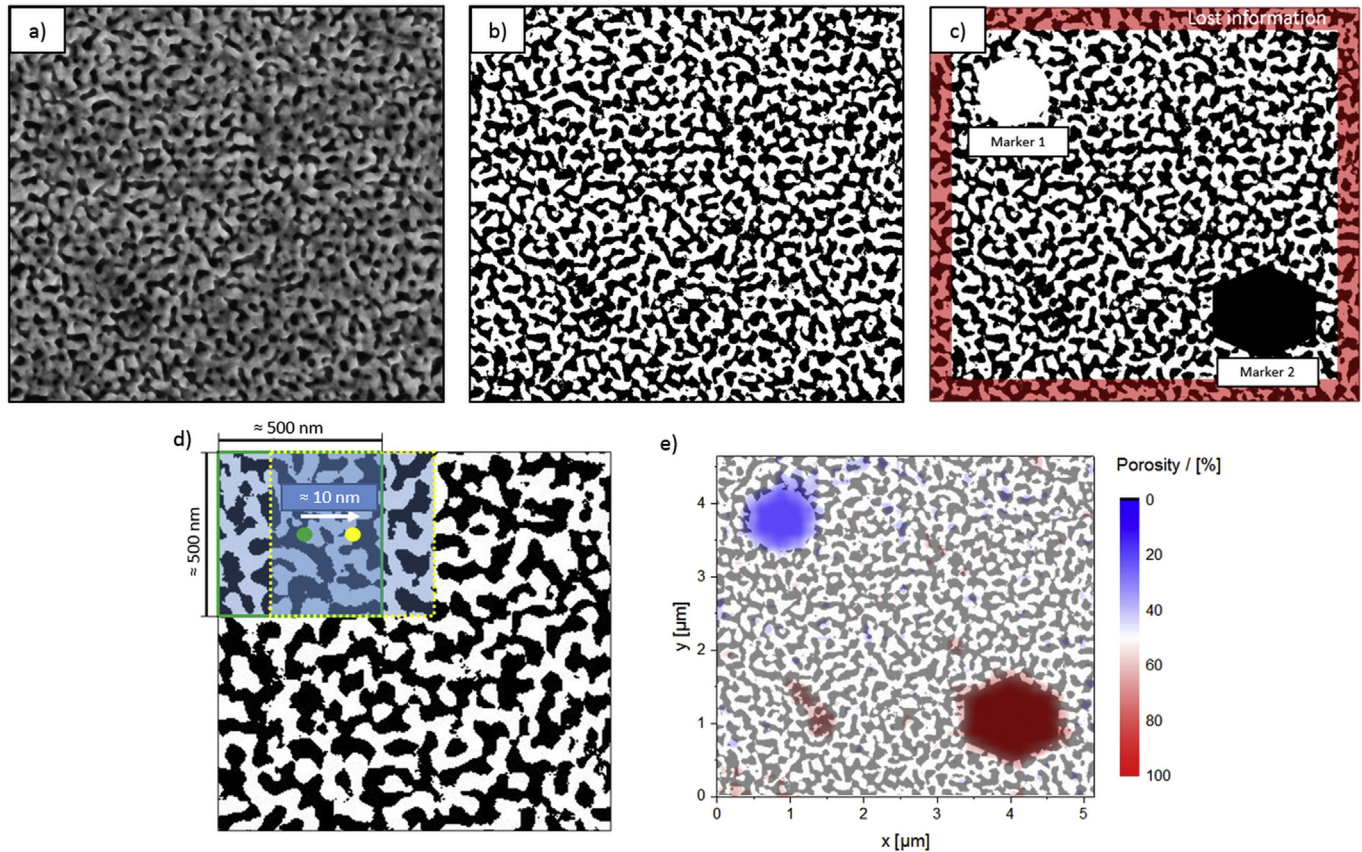
Fig. 5. Determination of localized porosity variations in NP Au. a) SEM micrograph of NP Au and b) binary image generated with python. c) Artificial markers and lost information at the outer border. d) Magnified visualization of the scanning procedure. e) Resulting porosity map with overlaid binary image which illustrates the local material porosity.
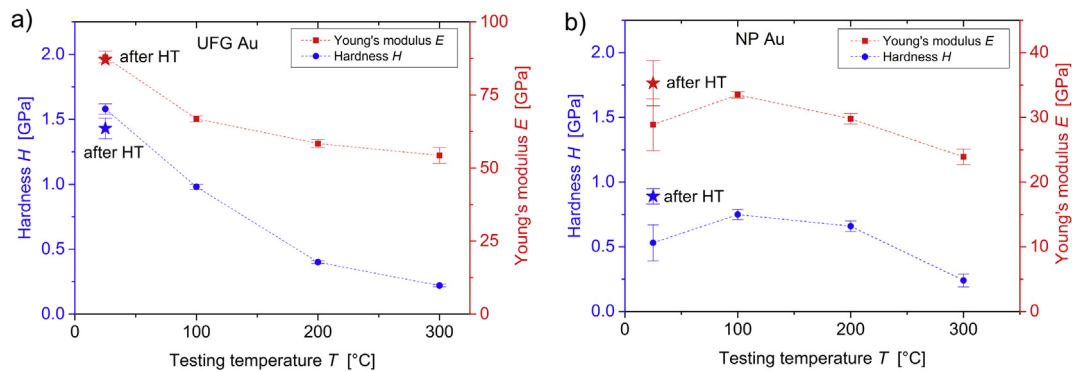

Fig. 6. Hardness and Young's modulus in the tested temperature range for both sample types a) UFG Au and b) NP Au. Star symbols mark the corresponding values measured again at RT after HT testing.

after HT experiments, the Young's modulus appears unaltered. H on the other hand slightly decreases.

The initial hardness of NP Au measured prior to HT experiments reveals values with low deviations (<0.05 GPa) for every prepared disk itself, but varies between individual samples with $H = 0.53$ GPa ± 0.14 GPa. RT measurements after HT tests disclose a significant increased hardness of around 68% to 0.89 GPa ± 0.06 GPa. The hardness reaches higher levels than the RT material after increasing the temperature to 100 °C, and then shows a continuous decrease up to 300 °C, where H reduces to 0.24 GPa ± 0.05 GPa. E was determined to be 28.9 GPa ± 4.0 GPa at RT, slightly increases at 100 °C but then reverses the trend until finally ending up at 23.9 GPa ± 1.2 GPa at 300 °C, illustrated in Fig. 6b. Just as for H, an increase of E was observed when tests were conducted again at

ambient temperatures. The origin of this increase after annealing will be discussed later.

3.2. Strain-rate sensitivity and activation volume

As a matter of clearness, data of representative indents for each temperature condition are plotted in Fig. 7, instead of whole data sets. It is common practice to deduce deformation rate-dependent parameters from Norton plots (Fig. 7a and d), resulting from Equation (1). The graphs show that while the load is held constant, the tip sinks deeper into the material. As a consequence, the hardness and indentation strain-rate are reduced, as depicted in Fig. 4.

RT experiments on UFG Au (Fig. 7a) result in m values reaching from 0.06 up to 0.16 with rising dwell time and hence decreasing
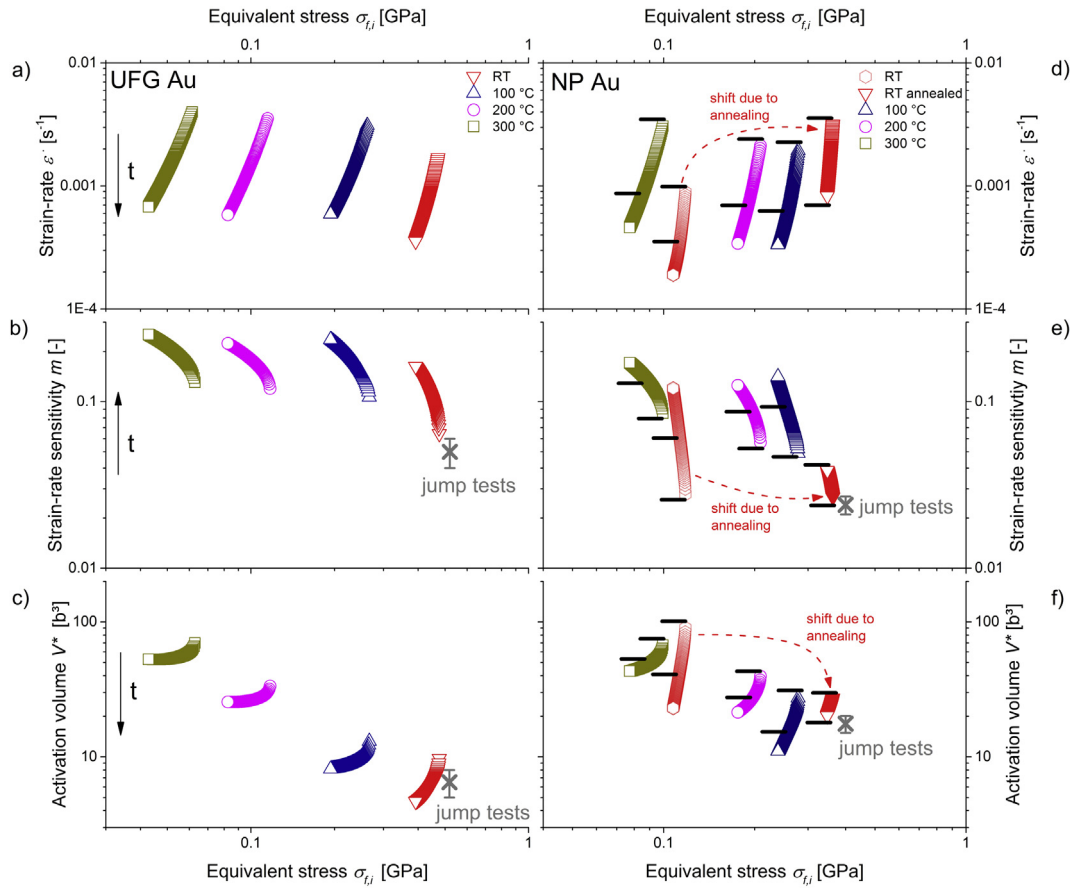
Fig. 7. Norton plot and corresponding diagrams of strain-rate sensitivity m and activation volume V^* in dependence of the equivalent indentation flow stress of indents at various temperatures for a)–c) UFG Au and d)–f) NP Au. In diagrams concerning NP Au, black lines indicate the first 30 s of the dwell time. A change in the RT behavior due to annealing of the foam is marked by a dashed-dot arrow. Increasing dwell time is marked by arrows on the left hand side. Additional RT strain-rate jump tests are in good agreement.

$\sigma_{f,i}$. When the samples are measured at HT, m shifts to slightly higher numbers accompanied by an expected reduction of $\sigma_{f,i}$, respectively (Fig. 7b). At 300 °C the maximum m value increases to 0.25. At RT V^* shows rather low numbers of less than 10 b^3 (Fig. 7c). V^* increases with ascending temperature up to 70 b^3 and becomes more independent of the indentation flow stress.

Aside from the mechanical strength of NP Au, m and V^* show a slight change too after the material was exposed to elevated temperatures. Results of tests at RT after annealing were obtained from 30 s dwell periods in contrast to the other tests, which were obtained from 200 s hold periods. For better comparability, the first 30 s of the 200 s dwell data were marked with black lines in Fig. 7d–f. At ambient temperature, m extends from values starting at around 0.03 and eventually ends up at 0.12. V^* results in values in the range between 23 b^3 and 90 b^3 at RT (Fig. 7f). After annealing, one can identify from Fig. 7e that m decreases to slightly lower values as does V^*. The increase in hardness after HT testing is recognized by the shift to higher indentation flow stresses.

High temperature experiments on the NP Au show a distinct rise of m compared to values after annealing. A further increase from 100 °C to 300 °C only causes a minor shift to higher m values, even though the flow stress decreases significantly (Fig. 7e). At 100 °C, V^* remains at a comparable level to RT, but clearly increases after further heating to 200 °C and 300 °C, eventually ending up in a maximum activation volume of 67 b^3.

The additional strain-rate jump tests carried out at RT are also indicated in Fig. 7, and those, considering the slightly higher strain-rates of $2.5 \cdot 10^{-2}$ s^{-1} to $5 \cdot 10^{-4}$ s^{-1}, are in good accordance with the data measured by the creep analysis, as expected from previous studies [22,41].

4. Discussion

In this chapter we will first compare our results of mechanical properties from static tests to existing literature data. After that, rate-dependent parameters will be discussed to draw conclusions regarding the governing dominant thermally activated deformation mechanism. Finally, we will visualize and examine the occurring deformation of NP Au by porosity maps and analyze their structure.

4.1. Mechanical properties

4.1.1. UFG Au

The RT hardness of UFG Au results in $H = 1.58 \pm 0.04$ GPa for the present 325 nm grain size material. In another study of HPT deformed UFG Au, a microhardness of 0.8 GPa was measured on samples with a mean grain size of 520 nm [49]. Hardness data obtained from nanoindentation of coarse grained (CG) Au shows values in the range between 0.8 GPa [50] and 2 GPa [51], whereat the latter value was measured at low indentation depths and will therefore underlie the indentation size effect [52]. However, considering the finer microstructure of the instant UFG Au due to the higher amounts of impurities as a result of the used powder route, well-known grain boundary hardening (Hall-Petch relation) [1,2] and solid solution hardening are a plausible explanation for the higher hardness. Similar trends have been noted for C impurities in Ni [53]. The measured Young's modulus with a value of 88.0 GPa $\pm$ 2.0 GPa is reasonable, as literature data varies between

57 GPa and 87 GPa depending on the crystal orientation [54–56]. Compared to CG metals, the UFG structure is known for a rapid decrease of H at elevated temperatures [57]. This has been observed for Al and Cu [58] and also goes along with observations of the present study, where UFG Au reaches lower hardness values at 300 °C compared to CG Au measured by Beake et al. at 400 °C [50]. While a slight decrease of E over T was expected, the present trend appears anomalous compared to bulk data [54], where E drops less than 10% in this temperature range. Such deviations might result from microstructural effects [59], even though a deviating frame compliance at HT cannot be excluded [50].

4.1.2. NP Au

To the best knowledge of the authors, NP Au has never been produced through powder consolidation, HPT processing and subsequent selective etching so far. Through this study, it can be validated that the described proceeding is suitable to fabricate NP Au with a unique microstructure. In contrast to porous Au made from Au/Ag precursors, where grains comprise several ligaments or the foam even features a single crystalline structure [5,8], the present foam differs in the grain size, which is about 70 nm in average when measured right after processing. For this reason, most of the ligaments contain more than one grain and consequently several grain boundaries. Therefore, it is not guaranteed that the values are non-restrictively comparable to literature data.

Following equation (4), one would estimate an indentation flow stress lower than 100 MPa for the foam, where the smaller structure size is already taken into account by applying the Hall-Petch law [1,2,23]. However, a far higher value of 212 MPa ± 56 MPa was measured in the present study, even further increasing to 356 MPa ± 24 MPa after annealing. Another approach is to rewrite equation (4) to solve for the flow stress of a corresponding bulk material. The flow stress of the ligament at RT prior HT tests results in 2.00 GPa ± 0.53 GPa. As mentioned before, after annealing the indentation flow stress increases to 3.36 GPa ± 0.22 GPa, a value approaching the theoretical strength of gold [56,60]. Various other studies on NP Au, using nanoindentation, observed ligament strengths in the same order of magnitude [6,7,9]. However, it has been noted that NP materials endure far lower stresses in tensile tests [8,61]. Tests with millimeter-sized samples on coarse grained and single crystalline nanoporous gold revealed a significantly lower yield strength of about 440 MPa [8], thereby most probably testing the material flaws rather than the intrinsic ligament strength.

The noticeable increase of H after HT tests, despite minor coarsening of the microstructure, suggest that the deformation behavior has changed. Recent investigations on severely plastically deformed metals reveal that annealing can cause an increase in hardness [3,4] due to annihilation of mobile dislocations and grain boundary relaxation [62]. Even though the relative increase of H is lower in the mentioned bulk studies (about 20%), the high fraction of free surface could promote the dislocation annihilation effect and therefore lead to a more pronounced hardening of the NP compared to UFG metals [63].

Recalculating the Young's modulus of the ligaments by using equation (5) results in $E = 116$ GPa ± 16 GPa. This does not accord well with studies by other authors, whose values obtained from equation (5) are conform with bulk data, assuming the Ashby equations still hold as an accurate approximation [5–7]. Taking into account the remaining iron by applying the rule of mixture proposed by Voigt [64] gives an estimate that the Young's modulus will be 10% higher compared to pure Au. Moreover, small deviations of the actual porosity at the imprint site can also lead to significant errors, since porosity enters the equation quadratically.

Even though the determined data for modulus and yield strength show similar results compared with literature data [5–10],

the analysis has to be critically reflected. One must keep in mind that the Ashby equations refer to macroscopic low density foams and do not take into account the more complex situation of the nanometer-sized microstructure, and consequently different conditions for dislocation motion. Anyway, by using the same equations as other authors previously, a comparison of values is certainly feasible, even though it cannot be guaranteed that these lead to the actual intrinsic mechanical properties of the ligaments. Rate-dependent properties, as discussed in the next chapter, may allow to indicate more directly if there are any distinct changes of the deformation mechanisms.

4.2. Strain-rate sensitivity and activation volume

At this point, some critical remarks shall be made regarding the testing technique. Since the used nanoindentation devices is not capable of performing dynamic indentation techniques such as continuous stiffness measurement, the sink-in depth h_s cannot be obtained continuously during the dwell period, but is calculated from the stiffness determined at the end of the hold segment. Another consequence of not using a dynamic indentation technique is that measurements are prone to thermal drift errors [22,41,59,65]. Even though a thermal drift rate is measured after 90% unloading, there is no guarantee that the linear correction accords with the actual drift during the test [41,59]. However, due to the short dwell time and comparison of h_s after shorter hold times, major deviations should be eliminated.

4.2.1. UFG Au

In general, a decreasing structure size in fcc metals is linked to an increase of m, which is in turn attributed to boundary/dislocation interactions [22,26,28]. Controversial results were published concerning the temperature dependence of V^*, where a decrease [24,66], as well as an increase [32,67] was observed for UFG and NC fcc materials at elevated temperatures.

The present study revealed increasing values for m and low values of V^* for UFG Au, which is in good accordance with studies on freestanding gold films [25,29]. Activation volumes in this order of magnitude are often referred to dislocation nucleation and accommodation processes at grain boundaries [24,27,68]. Similar values, obtained from nanoindentation strain-rate jump tests, were noted for other UFG fcc metals as well, such as Al and Ni [22]. At elevated temperatures, climb may enable dislocations to overcome obstacles, additionally favored by the high amount of high angle grain boundaries due to the HPT process [69]. Eventually, this results in a rising V^* with increasing temperature. Moreover, dislocation nucleation is favored by the induced thermal energy at HT, and a reduction of sub-grains at HT (Fig. 1a−d) will support the trend. In conclusion, V^* rises with increasing temperature and no profound changes of the deformation mechanism, e.g. towards diffusional deformation processes, are detected. Supersaturated Fe does not show a significant influence on the rate-dependent properties. At least the impact of remaining dissolved elements is hardly assessable with the methods applied in this study.

4.2.2. NP Au

The obtained values for m are linked to dislocation plasticity, where interaction with interfaces leads to a more strain-rate sensitive behavior [22,26,28]. A recent atomistic simulation study of NP Au demonstrated that perfect dislocations can occur even in ligaments with diameters down to 5 nm [70]. The reduction of V^* after HT tests fits into the concept that mobile dislocations may leave the material. Therefore, dislocations have to be nucleated either at free surfaces or from grain boundaries, both associated with low activation volumes [24,27,63,68], while prior to annealing

abundant dislocations are present in the ligaments and consequently enable an easier deformation. With increasing temperature, the nucleation of dislocations as well as their movement is supported by introduced thermal energy [68], therefore m and V^* show increasing values. The slight grain coarsening with temperature, displayed in Figs. 1 and 2, will promote an increase too because slip distance and dislocation length will increase. Besides common mechanisms described for UFG Au, it is conceivable that enhanced surface diffusion could contribute to a more rate-dependent behavior. Unfortunately, comparable literature data is lacking, since some of the required parameters which would certainly affect the obtained properties, such as porosity, ligament diameter, purity and microstructure, differ from other studies.

A different appearance of the deformed zone underneath indents that were conducted at different conditions could support the preceding assumption. Thus, FIB cross-sections of various indents were prepared and analyzed as described previously to give an insight on the occurring deformation.

4.3. Interpretation of appeared deformation of NP Au

The porosity maps displayed in Fig. 8 reveal a different appearance of the plastically deformed volume in NP Au at different temperature conditions. A distinct plastic deformation and densification, respectively, at highly stressed positions is obvious for indents made prior to HT tests (Fig. 8a), as one would expect for a foam. Through the densification the prescribed deformation can be accommodated in a small volume, resulting in a small plastic zone, as schematically depicted in Fig. 9a. However, this behavior changes significantly once the sample is exposed to HT, since in this condition the dislocation density is reduced (Fig. 9b). Instead of the local densification underneath the tip as seen for prior HT indents, slightly denser zones are emerging in an extended range of the cross-section (Fig. 8b). This suggests that deformation is localized in weak ligaments which presumably fail by slip events. Instead of a global densification by dislocation plasticity, weak ligaments close to the tip fail at first. If there are no more favorable ligaments around, the plastic deformation will be pushed farther away from the tip, ending up in an extended plastic zone (Fig. 9b). Once the induced stress is sufficient to nucleate dislocations at the surface or at interfaces, these can contribute again to meet the prescribed deformation. These observations coincide well with the obtained numbers for m and V^* indicating dislocation mediated processes. The reduction of V^* after annealing (Fig. 7f) suggests a shift from dislocation plasticity by pre-existing dislocations to a more nucleation controlled deformation behavior.

At higher temperatures a mixed state of deformation morphology was noticed (Fig. 8c and d). At 100 °C the extended plastic zone can clearly be seen by densified areas away from the tip, supporting the idea of an extended plastic zone in the annealed material. Densification occurs at some positions, but is not as homogenously distributed as in Fig. 8a. Available thermal energy can support nucleation of dislocations, and therefore account for an easier deformation during the tests. Interestingly, at 300 °C, when values for V^* are again similar to those of the prior-RT indent, the deformation appearance also becomes more alike again. At this temperature, dislocations can easily be nucleated and are able to contribute to a collective densification of the foam underneath the tip (Fig. 8d). Therefore, the assumption that the mechanical properties of the foam are strongly dependent on the presence of dislocations, appears to be justified. In-situ TEM studies could support this hypothesis, however, the nanocrystalline microstructure of the foam requires alignment of several $g \cdot b$ - conditions for each analyzed grain before and after, possibly even during annealing, which would be a very demanding task.

Contrary to the investigated UFG Au, where no distinct change of the deformation behavior was noted after annealing, these observations suggest that the high amount of free surfaces promotes an enormous hardening effect, given that the microstructure is temperature-stable as in the present case. Since no distinct coarsening of the ligaments was observed, it is unlikely that diffusional processes are the dominating deformation mechanism. Finally, we conclude that the deformation will mainly be governed by dislocation nucleation and accommodation processes for both materials, whereas the availability of free surfaces in the foam does not have a substantial impact on the rate-dependent parameters, or potentially the used method is not sensitive enough to assert clear differences. However, regarding the hardness of the materials the free surface plays a crucial role, since dislocations are able to leave the material during annealing. In contrast, in UFG Au the accommodation of dislocations will be restrained compared to NP Au since only grain boundaries are available as sinks for dislocations.

5. Summary and conclusions

UFG and NP Au, both based on the same raw material, were fabricated via HPT and subsequently investigated regarding their temperature- and rate-dependent deformation mechanisms. UFG Au revealed an average grain size of 325 nm, while the Au-Fe composite-derived Au foam offers a unique microstructure with a ligament diameter of around 100 nm, consisting of about 70 nm small grains in average (Figs. 1 and 2). A slight coarsening of the microstructure (reduction of sub-grains in the UFG materials, grain growth in the ligaments) was noted after the samples were exposed to elevated temperatures. Nanoindentation tests were performed from RT up to 300 °C (corresponding to a homologue temperature range of from 0.22 to 0.43) in order to obtain hardness H, Young's modulus E, strain-rate sensitivity m and activation volume V^*. In combination with implemented local porosity maps of FIB cross-sections of indents in NP Au, the following conclusions were drawn:

- UFG Au reveals a high hardness of 1.58 ± 0.04 GPa at RT, which is due to grain boundary and solid solution hardening. An increasing temperature leads to a rapid reduction of H (Fig. 6a), since climb of edge dislocations will be enhanced and favor easier deformation.
- For UFG Au, at RT V^* ($5\ b^3$–$10\ b^3$) is reduced and m (0.06–0.16) is clearly raised compared to conventionally grained materials, which can be associated with dislocation nucleation and accommodation processes. Both quantities increase at elevated temperatures (Fig. 7a–c), which can be referred to thermally activated climb of edge dislocations. Additionally, thermal energy will favor dislocation nucleation.
- It was noted that the hardness of NP Au significantly increased (~68%) after annealing (Fig. 6b). This goes along with a different appearance of the deformed volumes underneath nanoindents (Fig. 8). Such behavior could be caused by a significant reduction of mobile dislocations upon annealing of the foam, as dislocations are able to leave the material at free surfaces.
- The activation volume of NP Au decreases after the heat treatment from $23\ b^3$–$91\ b^3$ to $20\ b^3$–$27\ b^3$ at RT, while m slightly decreases from 0.030 to 0.053 to 0.027–0.038, again attributed to the reduction of mobile dislocations. Dislocation nucleation at free surfaces or grain boundaries, respectively, is required in order to deform the material. At HT m and V^* rise as nucleation will be supported by thermal energy (Fig. 7d–f). Diffusional processes seem not to be dominant since no distinct coarsening of the ligaments was noted.
- FIB cross-sections of NP Au prior and after HT testing (Fig. 8 a and b) affirm that the hardness increase is accompanied by a
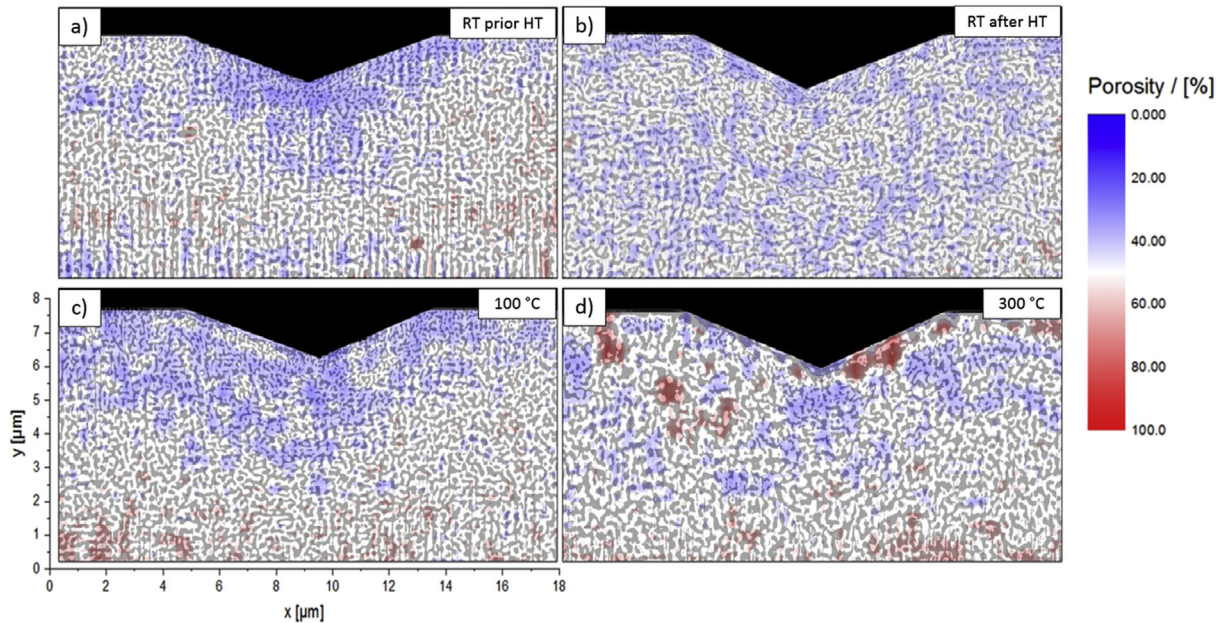
Fig. 8. FIB cross-sections of NP Au indents with overlaid porosity maps. a) Indent made right after processing at RT, b) RT indent after sample was exposed to elevated temperatures, c) indent made at 100 °C and d) at 300 °C.
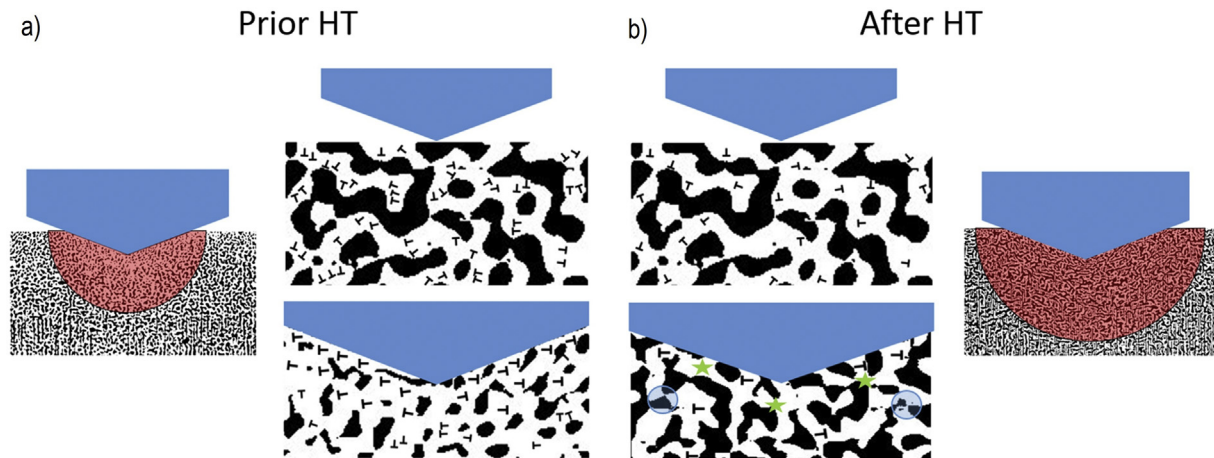

Fig. 9. Schematic illustration of different deformation mechanisms occurring in the NP Au. Slight transparent red semicircles indicate the plastically deforming zone. a) Prior to HT enough dislocations are present to evenly deform and densify the ligaments during indentation. b) After HT testing, very limited densification was noted. This suggests more localized failure of ligaments by local slip (blue circles) and the need of dislocation nucleation (green stars) in order to comply with the imposed deformation. (For interpretation of the references to colour in this figure legend, the reader is referred to the web version of this article.)

changing deformation appearance, in turn supported by changing rate-dependent properties. Cross-sections of indents conducted at HT show a mixed state of deformation morphology (Fig. 8c and d).

- In comparison, we conclude that the deformation of both tested materials is dominated by dislocation nucleation processes, whereas the presence of free surface in the NP Au leads to a similar rate dependent material behavior compared to UFG Au. In turn, the possibility for dislocations to leave the NP Au during annealing at free surfaces promotes a significant increase in hardness, shifting the deformation behavior from dislocation mobility controlled plasticity to a more nucleation-controlled mechanism.

Further investigations of the hardening effects will be necessary to understand the present processes in more detail. In particular, future in-situ TEM studies on the deformation behavior of NP Au could substantiate the details to the described dislocation behavior.

Appendix

A Fig. A1 demonstrates by example the reproducibility of nano-
indentation load-displacement curves for both materials, UFG
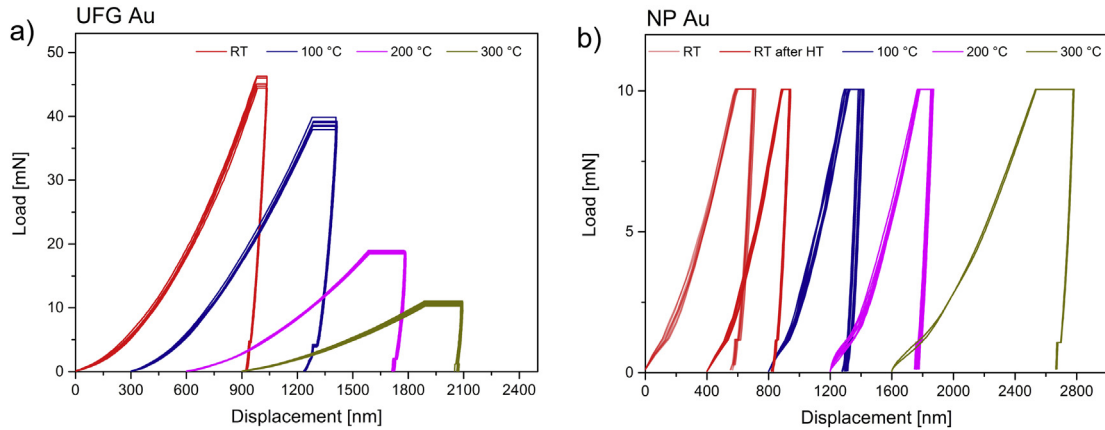Au and NP Au, at various temperatures.

Fig. A1. Load-displacement curves obtained by nanoindentation. a) Displacement-controlled tests on UFG Au and b) load-controlled tests on NP Au from RT to 300 °C. Note the offset of the curves for a better presentability.

Fig. B1 shows the original SEM micrographs of the prepared FIB cross-sections which were used for creating the density maps in Fig. 8.
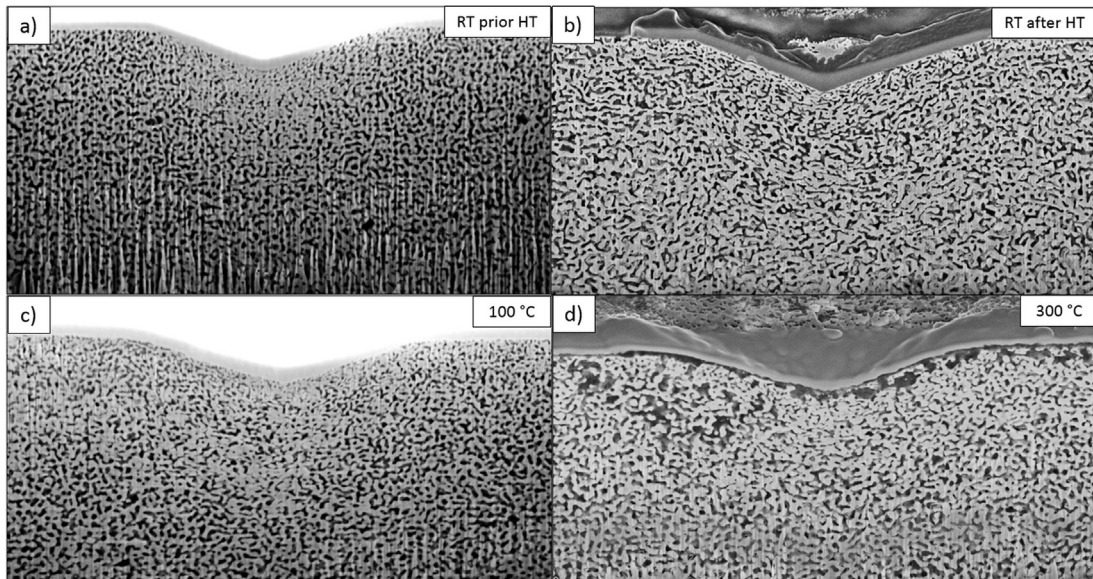

Fig. B1. a)–d) SEM images of the prepared FIB cross-sections of indents from different testing conditions.

In the following a short overview of the influence of parameters used for creating porosity maps will be given. Three parameters are investigated: threshold, step size and box size (see Fig. 5 for the analysis procedure).

Threshold: The conversion from greyscale to a b/w image re-
quires a threshold value which can be chosen in the interval of
0–255 due to the 8-bit greyscale format of the original image.
Fig. C1 shows the development of the relative density in a selected
box (see inset) in dependence of the threshold. Usually, the global
density is at least known in the range of ± 10%. In our case, this
would allow a threshold between 160 and 220. Fig C2 demonstrates
that, regardless of the chosen threshold the procedure can still
qualitatively differ denser from less dense regions, even though the
absolute density level naturally varies. If the deviation of the
porosity would be displayed relative to the determined mean
porosity, all images would have the same appearance but absolute
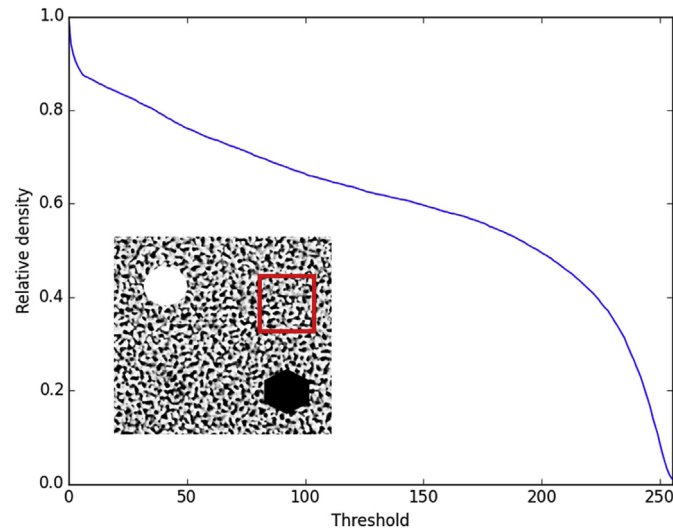values would be lost.

Fig. C1. Relative density in dependence of the threshold for the marked red box.
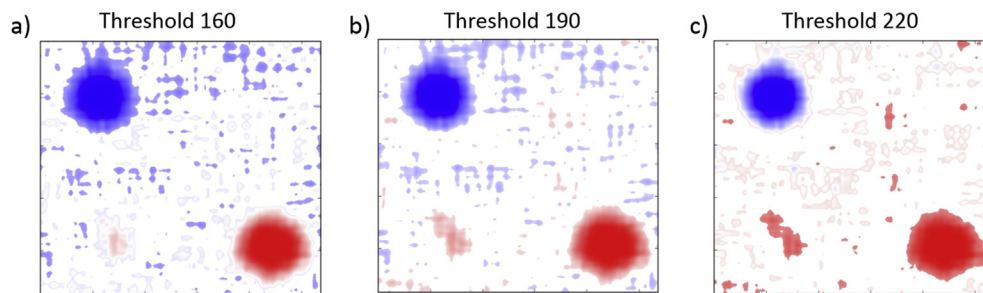

Fig. C2. Influence of threshold on obtained porosity maps. The maps depict absolute porosity values, which naturally vary with the threshold.

Box size: The used box should cover a representative area in regard to the microstructure. On the other hand, if size increases information and therewith local densification effects can be lost. For the present foam a box size of 500 nm was found sufficient to show the occurring densification zones. The influence of the box size on the porosity map appearance can be seen in Fig. C3.

Step size: The step size will determine the resolution of the image, seen in Fig. C4. The only advantage of larger step sizes is the lower processing time. Considering usual image sizes of around 2000 × 1500 px, this will end up in around 3,000,000 data points. Using a fast algorithm in the present study allows to obtain maximum resolution for all images, even though one can see that larger step sizes still give appropriate results.
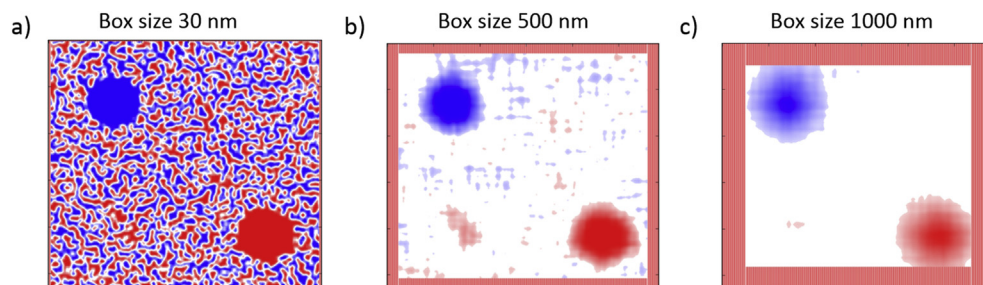

Fig. C3. Influence of the box size on obtained porosity maps. The zone of the indicated outer frame will be lost due to the box size.
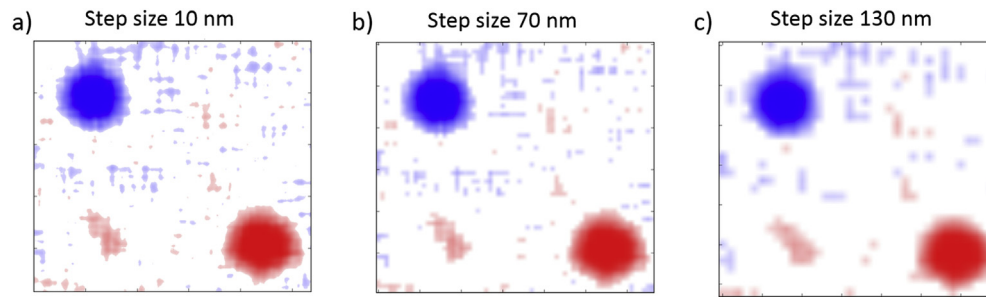
Fig. C4. Resultant porosity maps in dependence of the used step size. Details are lost for higher step sizes, but the map still gives an appropriate trend.

References

[1] E.O. Hall, The deformation and ageing of mild steel: discussion of results, Proc. Phys. Soc. Sect. B 64 (9) (1951) 747–753.

[2] N.J. Petch, The cleavage strength of polycrystals, J. Iron Steel Inst. 174 (1953) 25–28.

[3] X. Huang, N. Hansen, N. Tsuji, Hardening by annealing and softening by deformation in nanostructured metals, Science 312 (5771) (2006) 249–251.

[4] O. Renk, A. Hohenwarter, K. Eder, K.S. Kormout, J.M. Cairney, R. Pippan, Increasing the strength of nanocrystalline steels by annealing: is segregation necessary? Scr. Mater. 95 (0) (2015) 27–30.

[5] J. Biener, A.M. Hodge, A.V. Hamza, L.M. Hsiun, J.H. Satcher, Nanoporous Au: a high yield strength material, J. Appl. Phys. 97 (2) (2005) 024301.

[6] C.A. Volkert, E.T. Lilleodden, D. Kramer, J. Weissmüller, Approaching the theoretical strength in nanoporous Au, Appl. Phys. Lett. 89 (6) (2006) 061920.

[7] D. Lee, X. Wei, X. Chen, M. Zhao, S.C. Jun, J. Hone, E.G. Herbert, W.C. Oliver, J.W. Kysar, Microfabrication and mechanical properties of nanoporous gold at the nanoscale, Scr. Mater. 56 (5) (2007) 437–440.

[8] N.J. Briot, T. Kennerknecht, C. Eberl, T.J. Balk, Mechanical properties of bulk single crystalline nanoporous gold investigated by millimetre-scale tension and compression testing, Philos. Mag. 94 (8) (2014) 847–866.

[9] M. Hakamada, M. Mabuchi, Mechanical strength of nanoporous gold fabricated by dealloying, Scr. Mater. 56 (11) (2007) 1003–1006.

[10] A.M. Hodge, J. Biener, J.R. Hayes, P.M. Bythrow, C.A. Volkert, A.V. Hamza, Scaling equation for yield strength of nanoporous open-cell foams, Acta Mater. 55 (4) (2007) 1343–1349.

[11] D.M. Dimiduk, M.D. Uchic, T.A. Parthasarathy, Size-affected single-slip behavior of pure nickel microcrystals, Acta Mater. 53 (15) (2005) 4065–4077.

[12] M.D. Uchic, P. Shade, D.M. Dimiduk, Plasticity of micrometer-scale single crytstals in compression, Annu. Rev. Mater. Res. 39 (2009) 361–386.

[13] C.A. Volkert, E.T. Lilleodden, Size effects in the deformation of sub-micron Au columns, Philos. Mag. 86 (33–35) (2006) 5567–5579.

[14] M.D. Uchic, D.M. Dimiduk, J.N. Florando, W.D. Nix, Sample dimensions influence strength and crystal plasticity, Science 305 (5686) (2004) 986–989.

[15] J.R. Greer, W.D. Nix, Nanoscale gold pillars strengthened through dislocation starvation, Phys. Rev. B 73 (2006) 245410.

[16] E.M. Bringa, J.D. Monk, A. Caro, A. Misra, L. Zepeda-Ruiz, M. Duchaineau, F. Abraham, M. Nastasi, S.T. Picraux, Y.Q. Wang, D. Farkas, Are nanoporous materials radiation resistant? Nano Lett. 12 (7) (2012) 3351–3355.

[17] Z.W. Wang, Y.B. Wang, X.Z. Liao, Y.H. Zhao, E.J. Lavernia, Y.T. Zhu, Z. Horita, T.G. Langdon, Influence of stacking fault energy on deformation mechanism and dislocation storage capacity in ultrafine-grained materials, Scr. Mater. 60 (1) (2009) 52–55.

[18] I. Sabirov, Y. Estrin, M.R. Barnett, I. Timokhina, P.D. Hodgson, Tensile deformation of an ultrafine-grained aluminium alloy: micro shear banding and grain boundary sliding, Acta Mater. 56 (10) (2008) 2223–2230.

[19] R.W. Hayes, D. Witkin, F. Zhou, E.J. Lavernia, Deformation and activation volumes of cryomilled ultrafine-grained aluminum, Acta Mater. 52 (14) (2004) 4259–4271.

[20] N.Q. Chinh, P. Szommer, Z. Horita, T.G. Langdon, Experimental evidence for grain-boundary sliding in ultrafine-grained aluminum processed by severe plastic deformation, Adv. Mater. 18 (1) (2006) 34–39.

[21] T.G. Langdon, Grain boundary sliding revisited: developments in sliding over four decades, J. Mater. Sci. 41 (3) (2006) 597–609.

[22] V. Maier, B. Merle, M. Göken, K. Durst, An improved long-term nanoindentation creep testing approach for studying the local deformation processes in nanocrystalline metals at room and elevated temperatures, J. Mater. Res. 28 (9) (2013) 1177–1188.

[23] Y.H. Chew, C.C. Wong, F. Wulff, F.C. Lim, H.M. Goh, Strain rate sensitivity and Hall-Petch behavior of ultrafine-grained gold wires, Thin Solid Films 516 (16) (2008) 5376–5380.

[24] Y.M. Wang, A.V. Hamza, E. Ma, Temperature-dependent strain rate sensitivity and activation volume of nanocrystalline Ni, Acta Mater. 54 (10) (2006) 2715–2726.

[25] B. Merle, M. Göken, Bulge fatigue testing of freestanding and supported gold films, J. Mater. Res. 29 (2) (2014) 267–276.

[26] J. Chen, L. Lu, K. Lu, Hardness and strain rate sensitivity of nanocrystalline Cu, Scr. Mater. 54 (11) (2006) 1913–1918.

[27] A.T. Jennings, J. Li, J.R. Greer, Emergence of strain-rate sensitivity in Cu nanopillars: transition from dislocation multiplication to dislocation nucleation, Acta Mater. 59 (14) (2011) 5627–5637.

[28] Q. Wei, S. Cheng, K.T. Ramesh, E. Ma, Effect of nanocrystalline and ultrafine grain sizes on the strain rate sensitivity and activation volume: fcc versus bcc metals, Mater. Sci. Eng. A 381 (12) (2004) 71–79.

[29] R.D. Emery, G.L. Povirk, Tensile behavior of free-standing gold films. Part II. Fine-grained films, Acta Mater. 51 (7) (2003) 2079–2087.

[30] W.C. Oliver, G.M. Pharr, An improved technique for determining hardness and elastic modulus using load and displacement sensing indentation experiments, J. Mater. Res. 7 (6) (1992) 1564–1583.

[31] R. Schwaiger, B. Moser, M. Dao, N. Chollacoop, S. Suresh, Some critical experiments on the strain-rate sensitivity of nanocrystalline nickel, Acta Mater. 51 (17) (2003) 5159–5172.

[32] V. Maier, K. Durst, J. Mueller, B. Backes, H.W. Höppel, M. Göken, Nanoindentation strain-rate jump tests for determining the local strain-rate sensitivity in nanocrystalline Ni and ultrafine-grained Al, J. Mater. Res. 26 (11) (2011) 1421–1430.

[33] D. Peykov, E. Martin, R.R. Chromik, R. Gauvin, M. Trudeau, Evaluation of strain rate sensitivity by constant load nanoindentation, J. Mater. Sci. 47 (20) (2012) 7189–7200.

[34] Y. Liu, J. Hay, H. Wang, X. Zhang, A new method for reliable determination of strain-rate sensitivity of low-dimensional metallic materials by using nanoindentation, Scr. Mater. 77 (0) (2014) 5–8.

[35] R. Pippan, F. Wetscher, M. Hafok, A. Vorhauer, I. Sabirov, The limits of refinement by severe plastic deformation, Adv. Eng. Mater. 8 (11) (2006) 1046–1056.

[36] R. Pippan, S. Scheriau, A. Hohenwarter, M. Hafok, Advantages and limitations of HPT: a review, Mater. Sci. Forum 584–586 (2008) 16–21.

[37] M. Kreuzeder, M.-D. Abad, M.-M. Primorac, P. Hosemann, V. Maier, D. Kiener, Fabrication and thermo-mechanical behavior of ultra-fine porous copper, J. Mater. Sci. 50 (2) (2015) 634–643.

[38] A. Bachmaier, M. Kerber, D. Setman, R. Pippan, The formation of supersaturated solid solutions in Fe-Cu alloys deformed by high-pressure torsion, Acta Mater. 60 (3) (2012) 860–871.

[39] M.M. Primorac, M.D. Abad, P. Hosemann, M. Kreuzeder, V. Maier, D. Kiener, Elevated temperature mechanical properties of novel ultra-fine grained Cu-Nb composites, Mater. Sci. Eng. A 625 (0) (2015) 296–302.

[40] J.M. Wheeler, J. Michler, Indenter materials for high temperature nanoindentation, Rev. Sci. Instrum. 84 (10) (2013) 101301.

[41] K. Durst, V. Maier, Dynamic nanoindentation testing for studying thermally activated processes from single to nanocrystalline metals, Curr. Opin. Solid State Mater. Sci. 19 (6) (2015) 340–353.

[42] E.W. Hart, Theory of the tensile test, Acta Metall. 15 (2) (1967) 351–355.

[43] L.J. Gibson, M.F. Ashby, Cellular Solids: Structure and Properties, vol. 11, Cambridge University Press, 1997.

[44] D. Farkas, A. Caro, E. Bringa, D. Crowson, Mechanical response of nanoporous gold, Acta Mater. 61 (9) (2013) 3249–3256.

[45] T.J. Balk, C. Eberl, Y. Sun, K.J. Hemker, D.S. Gianola, Tensile and compressive microspecimen testing of bulk nanoporous gold, JOM 61 (12) (2009) 26–31.

[46] N. Mameka, K. Wang, J. Markmann, E.T. Lilleodden, J. Weissmüller, Nanoporous gold - testing macro-scale samples to probe small-scale mechanical behavior, Mater. Res. Lett. 4 (1) (2016) 27–36.

[47] L. Luehrs, C. Soyarslan, J. Markmann, S. Bargmann, J. Weissmüller, Elastic and plastic poisson's ratios of nanoporous gold, Scr. Mater. 110 (2016) 65–69.

[48] O.B. Olurin, N.A. Fleck, M.F. Ashby, Deformation and fracture of aluminium foams, Mater. Sci. Eng. A 291 (1–2) (2000) 136–146.

[49] K. Edalati, Z. Horita, High-pressure torsion of pure metals: influence of atomic bond parameters and stacking fault energy on grain size and correlation with hardness, Acta Mater. 59 (17) (2011) 6831–6836.

[50] B.D. Beake, J.F. Smith, High-temperature nanoindentation testing of fused silica and other materials, Philos. Mag. A 82 (10) (2002) 2179–2186.

[51] W.C. Oliver, R. Hutchings, J.B. Pethica, Measurement of hardness at indentation depths as low as 20 nanometers, Microindentation Tech. Mater. Sci. Eng. 889 (1986) 90–108.

[52] W.D. Nix, H. Gao, Indentation size effects in crystalline materials: a law for

strain gradient plasticity, J. Mech. Phys. Solids 46 (3) (1998) 411—425.

[53] G.B. Rathmayr, R. Pippan, Influence of impurities and deformation temperature on the saturation microstructure and ductility of HPT-deformed nickel, Acta Mater. 59 (19) (2011) 7228—7240.

[54] G. Simmons, H. Wang, Single Crytsal Elastic Constants and Calculated Aggregate Properties - A Handbook, MIT Press, Cambridge, 1971.

[55] H.E. Boyer, T.L. Gall, Metals Handbook, American Society for Metals, Ohio, 1985.

[56] J.D. Kiely, J.E. Houston, Nanomechanical properties of Au (111), (001), and (110) surfaces, Phys. Rev. B 57 (1998) 12588—12594.

[57] D. Caillard, J.L. Martin, Thermally Activated Mechanisms in Crystal Plasticity, vol. 8, Pergamon, 2003.

[58] B. Farrokh, A.S. Khan, Grain size, strain rate, and temperature dependence of flow stress in ultra-fine grained and nanocrystalline Cu and Al: synthesis, experiment, and constitutive modeling, Int. J. Plast. 25 (5) (2009) 715—732.

[59] V. Maier, A. Leitner, R. Pippan, D. Kiener, Thermally activated deformation behavior of ufg-Au: environmental issues during long-term and high-temperature nanoindentation testing, JOM 67 (12) (2015) 2934—2944.

[60] A. Stalder, U. Dürig, Study of yielding mechanics in nanometer-sized Au contacts, Appl. Phys. Lett. 68 (5) (1996) 637—639.

[61] K. Wang, A. Kobler, C. Kübel, H. Jelitto, G. Schneider, J. Weissmüller, Nano-porous-gold-based composites: toward tensile ductility, NPG Asia Mater. 7 (2015).

[62] T.J. Rupert, J.R. Trelewicz, C.A. Schuh, Grain boundary relaxation strengthening of nanocrystalline Ni-alloys, J. Mater. Res. 27 (2012) 1285—1294.

[63] R. Dou, B. Derby, Deformation mechanisms in gold nanowires and nanoporous gold, Philos. Mag. 91 (7—9) (2011) 1070—1083.

[64] W. Voigt, Über die Beziehung zwischen den beiden Elasticitätsconstanten isotroper Körper, Ann. Phys. 274 (12) (1889) 573—587.

[65] J.M. Wheeler, D.E.J. Armstrong, W. Heinz, R. Schwaiger, High temperature nanoindentation: the state of the art and future challenges, Curr. Opin. Solid State Mater. Sci. 19 (6) (2015) 354—366.

[66] T. Kunimine, T. Aragaki, T. Fujii, S. Onaka, M. Kato, Inverse temperature dependence of activation volume in ultrafine-grained copper processed by accumulative roll-bonding, J. Mater. Sci. 46 (12) (2011) 4302—4307.

[67] J.M. Wheeler, V. Maier, K. Durst, M. Göken, J. Michler, Activation parameters for deformation of ultrafine-grained Aluminum as determined by indentation strain rate jumps at elevated temperature, Mater. Sci. Eng. A 585 (0) (2013) 108—113.

[68] T. Zhu, J. Li, A. Samanta, A. Leach, K. Gall, Temperature and strain-rate dependence of surface dislocation nucleation, Phys. Rev. Lett. 100 (2008) 025502.

[69] J. Bach, J.P. Liebig, H.W. Höppel, W. Blum, Influence of grain boundaries on the deformation resistance: insights from an investigation of deformation kinetics and microstructure of copper after predeformation by ECAP, Philos. Mag. 93 (35) (2013) 4331—4354.

[70] C.J. Ruestes, D. Farkas, A. Caro, E.M. Bringa, Hardening under compression in Au foams, Acta Mater. 108 (2016) 1—7.